PHYSICAL REVIEW D **89**, 024014 (2014)

Solving the Hamiltonian constraint for $1 + \log$ trumpets

Tim Dietrich and Bernd Brügmann

Theoretical Physics Institute, University of Jena, 07743 Jena, Germany

(Received 20 September 2013; published 21 January 2014)

The puncture method specifies black hole data on a hypersurface with the aid of a conformal rescaling of the metric that exhibits a coordinate singularity at the puncture point. When constructing puncture initial data by solving the Hamiltonian constraint for the conformal factor, the coordinate singularity requires special attention. The standard way to treat the pole singularity occurring in wormhole puncture data is not generally applicable to trumpet puncture data. We investigate a new approach based on inverse powers of the conformal factor and present numerical examples for single punctures of the wormhole and $1 + \log$-trumpet type. Additionally, we describe a method to solve the Hamiltonian constraint for two $1 + \log$ trumpets for a given extrinsic curvature with a nonvanishing trace. We investigate properties of this constructed initial data during binary black hole evolutions and find that the initial gauge dynamics is reduced.

DOI: 10.1103/PhysRevD.89.024014 PACS numbers: 04.20.Ex, 04.25.D-, 04.25.dg, 04.30.Db

I. INTRODUCTION

A central issue in numerical general relativity is how to handle black holes and their spacetime singularities. In general, we can choose different foliations that avoid the singularities, either by explicit singularity excision [1] or by the puncture method [2–4], which leads to wormhole or trumpet slices that avoid the singularity automatically. The moving puncture method of [3,4] combines black hole punctures [2,5] with the Baumgarte-Shapiro-Shibata-Nakamura (BSSN) formalism [6,7] and appropriate gauge choices for the lapse [8] and the shift [9,10]. This leads to robust black hole simulations for a large variety of black hole systems. Most initial data for such configurations are created with the help of maximally sliced wormholes, e.g. [2,11,12]. When evolved with $1 + \log$ slicing by the moving puncture method, the wormholes lose contact with their second asymptotically flat end and are deformed into a trumpet (loosely speaking, "half" a wormhole) [13–16]. The quasiequilibrium state of a moving puncture is a trumpet. It is remarkable how quickly and robustly the gauge handles the transition from maximally sliced wormholes to $1 + \log$ sliced trumpets.

In this paper we address the question of how to compute trumpet initial data. It is a curious fact that we can easily obtain trumpets from wormholes by evolution, but there is no method yet to pose initial data representing two moving and spinning black holes by trumpets directly, without evolution, on appropriate slices in the $1 + \log$ gauge. Our analytic understanding of trumpets is restricted essentially to spherical symmetry, i.e. the Schwarzschild trumpet [13], for which both $1 + \log$ and maximal slicing is known [15,16,17]. Although puncture evolutions employ the $1 + \log$ gauge, so far most investigations of trumpet initial data beyond Schwarzschild have focused on maximally sliced trumpets [18–20]. Constant mean curvature slices with trumpets were considered in [21]. In [22] it is shown that constructing $1 + \log$ trumpet data for orbiting black holes may fail if one assumes the existence of a helical Killing vector, since in general such data are not asymptotically flat. However, this does not rule out the existence of asymptotically flat $1 + \log$ trumpet data that is only approximately stationary, which is the case we are interested in.

The goal in this paper is to analyze and resolve some of the difficulties that arise when solving the Hamiltonian constraint of the $3 + 1$ initial data problem for $1 + \log$ trumpets. We postpone the treatment of the momentum constraint. Let us summarize the key issues. Consider the conformal transverse-traceless (CTT) decomposition [23], where the physical metric is obtained by a conformal rescaling of a given background metric, $g_{ij} = \psi^4 \bar{g}_{ij}$, where $\psi > 0$ is the conformal factor. For puncture data we can assume that the metric is conformally flat. The basic feature is that the conformal factor has a coordinate singularity at $r = 0$, where r denotes the Cartesian distance to the puncture. Initial data for Schwarzschild can be written as wormhole puncture data with two asymptotic infinities, or as trumpet puncture data extending from a sphere with minimal area inside the horizon to infinity. The coordinate singularity for $r \to 0$ takes the form

$$\psi_{\mathrm{wormhole}} \sim \frac{1}{r} \qquad \psi_{\mathrm{trumpet}} \sim \frac{1}{\sqrt{r}}. \tag{1}$$

The above generalizes to more than one puncture by including a pole for each puncture. The Hamiltonian constraint for conformally flat initial data can be written as $\Delta\psi + F\psi^5 + G\psi^{-7} = 0$, with the boundary condition that $\psi \to 1$ as $r \to \infty$. Here Δ is the flat-space Laplace operator, and the functions F and G are obtained from the extrinsic curvature. Given the singular behavior of the conformal factor, Eq. (1), the question is how to compute such irregular solutions of the Hamiltonian constraint when a numerical solution is required.

For wormhole data with Bowen-York (BY) extrinsic curvature [24], a successful strategy [2] is to write the conformal factor as $\psi = \psi_S + u$ assuming $\Delta\psi_S = 0$ on $\mathbb{R}^3 \setminus \{0\}$, where ψ_S is the singular, but analytically known solution for vanishing extrinsic curvature for one or more punctures (the Brill-Lindquist conformal factor). We obtain a solution since $\Delta(1/r) = 0$ for $r \neq 0$. However, for trumpet data we encounter $\Delta(1/\sqrt{r}) \neq 0$. Furthermore, for $1 + \log$ trumpet data the trace of the extrinsic curvature, K, does not vanish. This introduces additional issues compared to maximal slicing, where $K = 0$.

In this paper we explore an alternative to $\psi = \psi_S + u$. Rather than attempting a split into singular and regular pieces, we consider a power of the inverse $1/\psi$ of the conformal factor [20,25]. For example, if $\psi \sim 1/\sqrt{r}$, then $\psi^{-4} \sim r^2$ is a regular function at the puncture. Introducing

$$\psi = f^p, \qquad p < 0, \tag{2}$$

for $p = -1/2$ we have $f_{\text{wormhole}} \sim r^2$, and for $p = -1/4$ we have $f_{\text{wormhole}} \sim r^4$ and $f_{\text{trumpet}} \sim r^2$; cf. (1).

The question is whether anything has been gained when writing the Hamiltonian constraint in terms of the new conformal factor f. Although taking the inverse of ψ to some power raises the differentiability at the puncture, *a priori* it is not clear whether the singularity has only been shifted to other terms. Indeed,

$$\Delta f^p = p f^{p-1}\left(\Delta f + (p-1)\frac{(\nabla f)^2}{f}\right). \tag{3}$$

The question is whether there are numerical issues for f approaching zero at the puncture, e.g. whether the numerical derivative in $\frac{(\nabla f)^2}{f}$ vanishes sufficiently fast for a regular result. Here $p = 1$, which corresponds to the power 4 in the conformal transformation of the metric, is precisely the choice that avoids first order derivatives in the Hamiltonian constraint. We will discuss how the numerical quality of the initial data depends on p.

Inverse powers of ψ have appeared in different contexts, for example, in black hole evolutions [3]. We suggested their use in the Hamiltonian constraint for the thesis of Gundermann [25]. That work focused on $1 + \log$ trumpets and on uniqueness issues of related model problems. For example, in a simple case ($F = \text{const}$) the solutions are not unique and two solutions were constructed explicitly. Some numerical experiments were performed in [25] as well, although a robust numerical implementation was missing. This is one of the goals of this paper.

Baumgarte [20] suggested the same approach with inverse powers of the conformal factor, as well as a working numerical scheme based on three-dimensional (3D) finite differences. The present paper and [20] are complementary in that we work with a 3D pseudospectral method that is a variant of [11]. A suitable numerical implementation that can handle possible regularity issues for the new conformal factor is found in both numerical approaches.

However, the major difference between the present work and other numerical studies of trumpet initial data [19,20,26,27] is that we do not assume maximal slicing (nor do we attempt to impose helical symmetry [22]). Instead of maximal trumpets with $K = 0$ and $F = 0$, we consider $1 + \log$ trumpets with $K \neq 0$ and $F \neq 0$, which adds the ψ^5 term in the Hamiltonian constraint.

The paper is organized as follows. In Sec. II we introduce the Hamiltonian constraint and discuss how the wormhole puncture method works and what the problems are extending this method to trumpets. In Sec. III we rewrite the Hamiltonian constraint with a regular conformal factor and describe some numerical calculations for a single wormhole, for a single $1 + \log$ trumpet, and for multiple $1 + \log$ trumpets. In Sec. IV we compare evolutions starting with the standard maximal wormhole data, with maximal trumpet data, and with the new $1 + \log$ trumpet data. We conclude in Sec. V.

II. HAMILTONIAN CONSTRAINT FOR PUNCTURES

A. Hamiltonian constraint

The standard $3 + 1$ decomposition [23] is formulated in terms of a three-metric g_{ij} and its extrinsic curvature K_{ij}. The Hamiltonian constraint for vacuum is

$$R(g) + K^2 - K_{ij}K^{ij} = 0, \tag{4}$$

where $R(g)$ is the Ricci scalar of g_{ij}, and $K = g^{ij}K_{ij}$ is the trace of the extrinsic curvature. The CTT decomposition introduces a conformal factor $\psi > 0$ such that the "physical" metric g_{ij} is obtained from the "conformal" metric $\bar{g}_{ij}$ by

$$g_{ij} = \psi^4 \bar{g}_{ij}. \tag{5}$$

We could insert (2) here, $g_{ij} = f^{4p}\bar{g}_{ij}$, but we may as well insert the new conformal rescaling in the final decomposition so that we do not have to repeat the standard calculations. Since

$$R(\psi^4\bar{g}) = \psi^{-4}R(\bar{g}) - 8\psi^{-5}\bar{\Delta}\psi, \tag{6}$$

the Hamiltonian constraint for the conformal variables becomes

$$\bar{\Delta}\psi - \frac{1}{8}R(\bar{g}_{ij})\psi + \frac{1}{8}(K_{ij}K^{ij} - K^2)\psi^5 = 0, \tag{7}$$

where the Laplace operator $\bar{\Delta}$ refers to the conformal metric. When constructing initial data, $\bar{g}_{ij}$ is considered given while ψ is determined as a solution of (7). For puncture data we assume that the conformal metric is flat, which implies $R(\bar{g}_{ij}) = 0$. We drop the overhead bar to simplify our notation when it is evident that we are referring to the conformal variables.

The CTT decomposition also introduces the trace-free part of the extrinsic curvature, $A_{ij} = K_{ij} - g_{ij}K/3$, and the conformal transformation

$$A_{ij} = \psi^{-2}\bar{A}_{ij}, \qquad K = \bar{K}. \tag{8}$$

In this work we do not address the question of how to solve the momentum constraint. Instead we consider examples where the extrinsic curvature is given, either as an explicit solution to the momentum constraint, or as an approximation that does not solve the momentum constraint, but that provides an initial guess for its solution at a later stage.

In the following we consider the Bowen-York extrinsic curvature, for which $K = 0$, as well as $1 + \log$ trumpet data, for which $K \neq 0$. The Hamiltonian constraint takes the form

$$\Delta\psi + F\psi^5 + G\psi^{-7} = 0. \tag{9}$$

For the Bowen-York extrinsic curvature, $F = 0$ and $G = \bar{A}_{ij}\bar{A}^{ij}/8$. For trumpet data, we can set $F = (K_{ij}K^{ij} - K^2)/8$ and $G = 0$ without performing the trace decomposition, or $F = -K^2/12$ and $G = \bar{A}_{ij}\bar{A}^{ij}/8$. Furthermore, one could also add Bowen-York extrinsic curvature to trumpet data in order to imbue the trumpet with linear and angular momentum.

B. Wormhole puncture

The original puncture method is motivated by the Schwarzschild metric in spatially isotropic coordinates on slices of constant Schwarzschild time. The metric is conformally flat with vanishing extrinsic curvature,

$$\psi = \psi_S = 1 + \frac{m}{2r}, \qquad g_{ij} = \psi_S^4\delta_{ij}, \qquad K_{ij} = 0. \tag{10}$$

The conformal factor is the fundamental solution of the (flat-space) Laplace equation,

$$\Delta\psi = 0, \tag{11}$$

on a “punctured” $\mathbb{R}^3$, i.e. $\mathbb{R}^3$ without the puncture point $r = 0$, subject to the boundary condition $\psi(\infty) \equiv \lim_{r\to\infty}\psi = 1$. As a function on $\mathbb{R}^3$, ψ has a coordinate singularity at $r = 0$. In terms of the Schwarzschild radial coordinate R; however, we have the geometric picture of a wormhole between two asymptotically flat regions that is isometric about the horizon at $r = m/2$, $R = 2m$. As r ranges from 0 to ∞, R drops from ∞ at the inner asymptotically flat end to a minimum at the throat for $R = 2m$ before growing again to ∞ at the outer asymptotically flat end.

If we consider a puncture with Bowen-York extrinsic curvature, then we have to solve

$$\Delta\psi + G\psi^{-7} = 0, \tag{12}$$

where $G = O(r^{-6})$ if there is spin, and $G = O(r^{-4})$ if there is linear momentum. While analytically not an issue (e.g. existence and uniqueness can be proven), the question is how to treat the coordinate singularity at the puncture numerically.

The original puncture method of [2,28–30] proceeds by considering

$$\psi = \psi_S + u, \tag{13}$$

$$\Delta u + G(\psi_S + u)^{-7} = 0, \tag{14}$$

$$u(\infty) = 0. \tag{15}$$

The key observation is that there exists a unique regular solution u on (the unpunctured) $\mathbb{R}^3$. Put simply, we can solve for a regular function u on the entire $\mathbb{R}^3$, add it to the singular background solution ψ_S for vanishing extrinsic curvature, and obtain a solution with spin and momentum. Since the pole of ψ_S has been handled analytically by using $\Delta\psi_S = 0$ in the transition from (12) to (14), we do not expect and in practice do not encounter numerical difficulties when solving (14) for u.

Although the “puncture trick” (13)–(14) is straightforward as presented, some of its features should be recalled since they are relevant to the construction of trumpet data. Obviously the puncture method depends on the existence of an analytic solution for the Schwarzschild solution. By using ψ_S or its immediate generalization to multiple Brill-Lindquist punctures, we enforce the existence of black holes in the data. The treatment of the puncture point is somewhat subtle. First we discover solutions to (11) or (12) that have a pole at $r = 0$, introduce $u = \psi - \psi_S$ on $\mathbb{R}^3 \setminus \{0\}$, realize that u is uniquely determined on $\mathbb{R}^3$ by (14) (where we have compactified the inner infinity), and declare this to be the unique solution we want. In technical terms, there is a removable singularity at $r = 0$. However, by choosing the unique extension we also make a choice about the inner boundary. From the point of view of the wormhole construction, we could be working on $\mathbb{R} \times S^2$ with $\psi = 1$ at both asymptotic ends, but this would not automatically build in a black hole of mass m.

Other features of the puncture solution depend on the choice of extrinsic curvature. For $G = O(r^{-6})$, we find that with $\psi = O(r^{-1})$ the nonprincipal terms in (12) are $G\psi^{-7} = O(r) \in C^0$, i.e. continuous, and a solution u of (12) is therefore expected to be twice differentiable at the puncture, $u \in C^2$ [2]. This is sufficient for second order finite differences, but we have to expect numerical issues for higher order approximations. In practice some higher order difference schemes can be applied to improve accuracy, e.g. [31]. Furthermore, a coordinate transformation can raise the differentiability at the puncture to C^∞, so a pseudospectral method can show exponential convergence [11]. Depending on the extrinsic curvature, there may be issues with the uniqueness (and/or existence) of solutions to the Hamiltonian constraint. Essentially, for $K \neq 0$ there is no general theorem for existence and uniqueness of the full set of constraints in the asymptotically flat setting, but given a concrete choice of K_{ij}, some statements can be made [30].

C. Trumpet puncture

A key difference when working with non-Bowen-York–type extrinsic curvature and/or changing the boundary conditions of the Hamiltonian constraint is the possibility that the singularity of the conformal factor at the puncture changes. For wormholes $\psi \sim 1/r$, while for standard trumpets $\psi \sim 1/\sqrt{r}$. Geometrically, a trumpet is one-half of a wormhole. The puncture point $r = 0$ corresponds to a finite value of the Schwarzschild radial coordinate $R(r)$, $R(0) = R_0$.

Consider the $1 + \log$ trumpet for the Schwarzschild spacetime that arises in puncture evolutions with the moving puncture gauge, where $R_0 \approx 1.312M$. The extrinsic curvature terms in the Hamiltonian constraint (9) assume a finite value, i.e. $G = 0$ and $F = (K_{ij}K^{ij} - K^2)/8$, $F_0 > 0$, and in particular $K_0 \approx 0.3009M^{-1}$. If we make the ansatz that ψ behaves like some power of r at the puncture, and that F approaches a constant F_0, then by simple power counting using (9),

$$\psi \sim r^q, \qquad \Delta\psi \sim \psi^5 \to r^{q-2} \sim r^{5q} \to q = -\frac{1}{2}. \tag{16}$$

Detailed calculations confirm this behavior [13].

Although not trivially given as in the case of a Schwarzschild wormhole, we can compute

$$\psi = \psi_{\text{trumpet}}, \qquad F = F_{\text{trumpet}} \tag{17}$$

semianalytically at the cost of a one-dimensional integration; see [32,33] and Sec. III C. For the numerical computation of trumpet data, we therefore do have a similar starting point as in the case of wormhole data; i.e. we are given the Schwarzschild case. The question is how we can extend the Schwarzschild trumpet to the spinning/moving case and the case of multiple punctures. The catch is that now the Schwarzschild solution does not drop out trivially when making the ansatz

$$\psi = \psi_{\text{trumpet}} + u, \tag{18}$$

since $\Delta\psi_{\text{trumpet}} = -F_{\text{trumpet}}\psi^5_{\text{trumpet}}$ does not vanish but rather gives a curvature term. Consider for example two Schwarzschild punctures (no spin, no momentum) at different locations with two solutions

$$\Delta\psi_{(n)} + F_{(n)}\psi^5_{(n)} = 0. \tag{19}$$

If we set

$$\psi = \psi_{(1)} + \psi_{(2)} + u, \tag{20}$$

then the Hamiltonian constraint becomes

$$\begin{aligned}\Delta u &= \Delta\psi - \Delta\psi_{(1)} - \Delta\psi_{(2)} \\ &= -F(u + \psi_{(1)} + \psi_{(2)})^5 + F_{(1)}\psi^5_{(1)} + F_{(2)}\psi^5_{(2)}.\end{aligned} \tag{21}$$

For wormhole punctures with Bowen-York extrinsic curvature, the corresponding right-hand side of (21) would be nonsingular and the coefficient would vanish sufficiently fast at the punctures such that $u \in C^2$. However, for trumpet punctures the leading order behavior is determined by the $\psi^5 \sim r^{-5/2}$ terms. We assume not only that the $F_{(n)}$ are nonzero but also that the combined F is nonzero at the puncture, and that there are no unexpected cancellations in (21). Then we conclude that u is as singular as ψ, i.e. $u \sim r^{-1/2}$, and we have not gained regularity for the numerical solution. This means that the additive correction of the original puncture trick as given in (20) is not sufficient for $1 + \log$ trumpets. Rather, we should look for a different way to handle the $r^{-1/2}$ singularity at the puncture.

It is possible to move parts of the singularity into the analytic part of the conformal factor, as done for maximal trumpets in [15,19], and this approach could be attempted for $1 + \log$ trumpets as well. As an alternative we considered a multiplicative puncture trick, $\psi = \psi_S\chi$, where ψ_S contains the singular part. Numerical experiments with this ansatz were successful, but the accuracy was several orders of magnitude lower than for (2). We did not pursue this option further. Let us mention that [27] had some success with transforming the radial coordinate by $s = \sqrt{r}$.

The proposal in the present work is to insert (2), $\psi = f^p$, into the Hamiltonian constraint (9), which with (3) leads to

$$\Delta f - (p-1)\frac{(\nabla f)^2}{f} + \frac{F}{p}f^{4p+1} + \frac{G}{p}f^{-8p+1} = 0. \tag{22}$$

We have normalized the principal part, as is customary and often advantageous for a numerical implementation. As examples we consider a wormhole puncture with BY extrinsic curvature for $p = -\frac{1}{2}$, $f \simeq r^2$,

$$\Delta f - \frac{3}{2}\frac{(\nabla f)^2}{f} - 2Gf^5 = 0, \tag{23}$$

and the $1 + \log$ Schwarzschild trumpet for $p = -\frac{1}{2}, -\frac{1}{4}, -\frac{1}{8}$, and $f \simeq r, r^2, r^4$,

$$\Delta f - \frac{3}{2}\frac{(\nabla f)^2}{f} - 2Ff^{-1} - 2Gf^5 = 0, \tag{24}$$

$$\Delta f - \frac{5}{4}\frac{(\nabla f)^2}{f} - 4F - 4Gf^3 = 0, \tag{25}$$

$$\Delta f - \frac{9}{8}\frac{(\nabla f)^2}{f} - 8Ff^{1/2} - 8Gf^2 = 0, \tag{26}$$

respectively. The leading order behavior of the terms with derivatives is therefore r^{-1}, 1, or r^2. In all cases the division of a numerical derivative by f in $\frac{(\nabla f)^2}{f}$ may or may not be numerically tricky. Furthermore, we have to discuss the regularity of the terms Ff^{4p+1} and Gf^{-8p+1}. A difference between maximal and 1+log trumpets is $F \neq 0$ ($K \neq 0$). While Gf^{-8p+1} vanishes sufficiently rapidly for our choices of p, Ff^{4p+1} contributes at the same leading order as the derivative terms. The different values of p are chosen to examine whether increasing the smoothness of $f \simeq r^{-1/(2p)}$ near the puncture helps, but it turns out that increasing the order in r can be detrimental. Equation (25), $f \simeq r^2$, was one of the examples considered in [25], since with $-4Ff^0 = K^2/3 \simeq$ const the nonvanishing K enters in a rather simple manner. The first impression that F/f in (24) will cause problems when computing the right-hand side turns out to be wrong. In our examples, $p = -\frac{1}{2}$ leads to the most accurate results.

III. SOLVING THE HAMILTONIAN CONSTRAINT WITH REGULAR CONFORMAL FACTOR

A. Numerical method

To test the method we use a new implementation of the single domain pseudospectral code of [11], which is described in [34] in more detail. The goal was not to obtain exponential convergence, but rather to employ an existing, efficient method that can be expected to show polynomial convergence even in the presence of the trumpet singularity. Since the required grid size turns out to be rather small (a 3D or 2D grid with no more than 10,000 points total), we can use a direct linear matrix solver inside a Newton-Raphson iteration.

For the single puncture we introduce compactified spherical coordinates (A, θ, φ), where we have compactified according to

$$A = \left(1 + \frac{m}{2r}\right)^{-1}. \tag{27}$$

The computational domain consists of a Chebychev grid in the radial direction and two Fourier grids for the angular quantities, which we denote as a Chebychev-Fourier-Fourier grid (an alternative to spherical harmonics, e.g. [35–37]). For the collocation points we choose the staggered Chebychev grid that does not include points at the boundary, i.e. the zeros of the Chebychev polynomials $T_{n_A}(1 - 2A)$, $\sin(n_\theta \theta)$, and $\sin(n_\varphi \varphi)$, where n_A, n_θ, n_φ denote the number of grid points in each direction. The puncture is located on the (two-dimensional) $A = 0$ boundary. This improves the convergence behavior of the spectral method, because no kink or pole is located in the interior of the grid. As a consequence of the staggering, we avoid outright division by zero at the puncture, although some numerical issues remain as the points cluster quadratically near $A = 0$. On the other hand, we cannot impose a Dirichlet boundary condition at infinity trivially since the grid is staggered there as well. We implement the outer boundary at $A = 1$ by extrapolation (which in our case gives more accurate results than the variable substitution described in [11]).

For two punctures we introduce compactified prolate spheroidal coordinates, in our notation (A, B, φ), with the inverse coordinate transformation to Cartesian coordinates given by

$$x = b\frac{A^2 + 1}{A^2 - 1}\frac{2B}{1 + B^2}, \tag{28}$$

$$y = b\frac{2A}{1 - A^2}\frac{1 - B^2}{1 + B^2}\cos(\varphi), \tag{29}$$

$$z = b\frac{2A}{1 - A^2}\frac{1 - B^2}{1 + B^2}\sin(\varphi). \tag{30}$$

This coordinate transformation was introduced for wormhole initial data in [11]. It was shown that there is a correction u that is C^∞ at the punctures. The computational domain is built up of either a Chebychev-Chebychev-Fourier (CCF) or a Chebychev-Fourier-Fourier grid (CFF). The grid points for the CCF grid are the zeros of $T_{n_A}(1 - 2A)$, $T_{n_B}(-B)$, and $\sin(n_\varphi \varphi)$. The radial-type coordinate is again denoted by A with $A = 1$ at spatial infinity. The coordinate B runs from -1 to 1, and the two punctures are located at $A = 0$, $B = \pm 1$. Thus, the black holes are at (one-dimensional) edges of the grid. As for the single puncture we extrapolate to spatial infinity. For the CFF grid we introduced a double covering in B, where B runs from -2 to 2, and the first black hole is at $A = 0$, $B = 0$ and the second at $A = 0$, $B = \pm 2$. The grid points are the zeros of $\sin(\frac{\pi}{2} n_B B)$.

B. Single wormhole

For a single wormhole with a regular conformal factor, we have $K = 0$ and thus $F = 0$, while $\bar{A}_{ij}\bar{A}^{ij}$ is defined by the Bowen-York curvature

$$\bar{A}_{ij} = \frac{3}{2r^2}\bigg(n_i P_j + n_j P_i + n_k P^k(n_i n_j - \delta_{ij}) - \frac{3}{r^3}(\varepsilon_{ilk} n_j + \varepsilon_{jlk} n_i) n^l S^k\bigg), \tag{31}$$

where P^i is the momentum and S^k the spin of the black hole. The outward-pointing unit radial vector is denoted by n^i. As described in the Introduction, wormhole initial data are widely used in numerical relativity, but solving the Hamiltonian constraint for wormholes considering a regular factor is a novel idea; see also [20].

For the computation of the regular factor f we have to define two boundaries. One is the outer boundary, where we set $f|_\infty = 1$, and the other refers to the puncture point. In the standard puncture method the inner boundary condition is not needed, because the mass of the black hole is imposed via $\psi_S = 1 + \frac{m}{2r}$. For the regular conformal factor, the mass of the black hole is not fixed, so we find an entire branch of solutions, making the numerical code fail (the linear problem is underdetermined) unless we impose the mass of the wormhole by hand. This is to be expected; see Sec. II B. For $p = -1/2$, we impose a condition on the second derivative of f at the puncture. We set $\partial_A^2 f = 2$, so that $f \sim A^2$ near the puncture. It is straightforward to see that this also holds for BY extrinsic curvature. The mass scale is then given by m in the definition of A; see (27). With the correct boundary condition, the method solves the Hamiltonian constraint for the Schwarzschild wormhole for vanishing extrinsic curvature without problems and obtains a numerical approximation to $f_S = \psi_S^{-2}$ with a rather smooth numerical error; see Fig. 1. In particular, there are no numerical artifacts at the puncture. We have confirmed that the method also works for single wormholes with BY extrinsic curvature for spin and linear momentum.

C. Single 1 + log trumpet

When solving (22) for a single trumpet, we can compare our results with the semianalytical known solution.

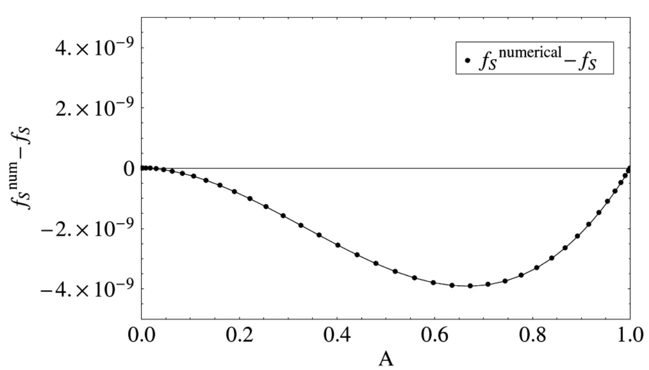

FIG. 1. Single wormhole, Schwarzschild solution. Difference between the numerical result for the regular conformal factor f obtained with the pseudospectral code for $n_A = 40$, $n_\theta = 2$, $n_\phi = 1$ and the analytical solution.

We integrate the $1 + \log$ condition as in [33], obtaining with $S = 1/R$

$$F(S,\alpha) \equiv \alpha^2 - 1 + 2S - Ce^\alpha S^4 = 0, \tag{32}$$

$$\frac{\partial F}{\partial S} = 2 - 4Ce^\alpha S^3, \tag{33}$$

$$\frac{\partial F}{\partial \alpha} = 2\alpha - Ce^\alpha S^4. \tag{34}$$

We compute $S(\alpha)$ with the Newton-Raphson method, and from

$$\frac{dS}{dr} = -\frac{S(r)}{\alpha(S(r))} r \tag{35}$$

we obtain

$$\psi^{-2}(r) = \frac{r}{R(r)}. \tag{36}$$

Figure 2 is a comparison between the results achieved by our single domain pseudospectral code and the semianalytical solution (36). The upper panel shows that our code finds the correct solution. This was not clear from the beginning because of uniqueness issues revealed by [25]. But since we are interested in ψ, $f > 0$, a power series expansion can be used to visualize why it is likely to find the correct solution with an appropriate initial value close to the analytical solution [34].

According to the lower panel of Fig. 2 the method does not achieve exponential convergence, except perhaps for small n_A, but this behavior was expected. On the one hand, we have regularity issues at the puncture, and on the other hand, there may be logarithmic terms at spatial infinity. Both effects lead to polynomial convergence of the pseudospectral code, which should explain the observed polynomial order of about 5. More important is the qualitative difference between the choices of p. As mentioned in Sec. II C, regarding the regularity of Ff^{4p+1} one might expect that $p = -1/2$ can cause difficulties because of the division by f. However, Fig. 2 indicates that $p = -1/2$ gives more accurate solutions than $p = -1/4$, while $p = -1/8$ is significantly less accurate than both these choices. The reason for this could be that a linear function does not require as much numerical resolution as a quadratic or quartic function, which explains why the results for $p = -1/2$ are better than for the others. Although $\frac{(\nabla f)^2}{f}$ is analytically zero at the puncture for $p = -1/4$ or $p = -1/8$, there are indications that with an increasing exponent of r some accuracy is lost.

Figure 3 shows the logarithm of the error with respect to the semianalytical solution for $p = -1/2$ and $p = -1/4$ versus A. Note the numerical noise for $p = -1/2$ near the

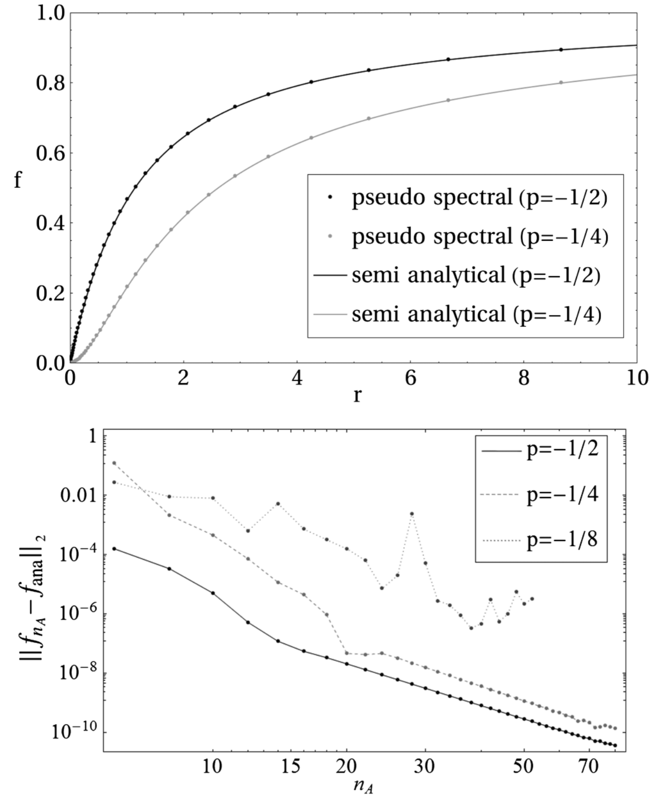

FIG. 2. Single $1 + \log$ trumpet, Schwarzschild solution. Comparison between the numerical and the semianalytical solutions (upper panel) for different choices of p, and a log-log plot of the convergence in the l_2 norm of the difference between the numerical and the semianalytical solution (lower panel). In the upper panel $n_A = 50$, and in both panels $n_\theta = 2$, $n_\phi = 1$. For large n_A there appears to be polynomial convergence of order 5 ± 0.5.

puncture ($A = 0$), which is likely due to the $1/r$ behavior of the Hamiltonian constraint, with additional issues near infinity ($A = 1$). For very high resolution, $n_A = 100$, there are numerical issues both at the puncture and at infinity even for $p = -1/4$. However, this resolution is significantly higher than in Fig. 2, and various numerical roundoff effects can make the error larger than for lower resolutions. Overall, an error on the order of 10^{-10} is certainly acceptable for our purpose.

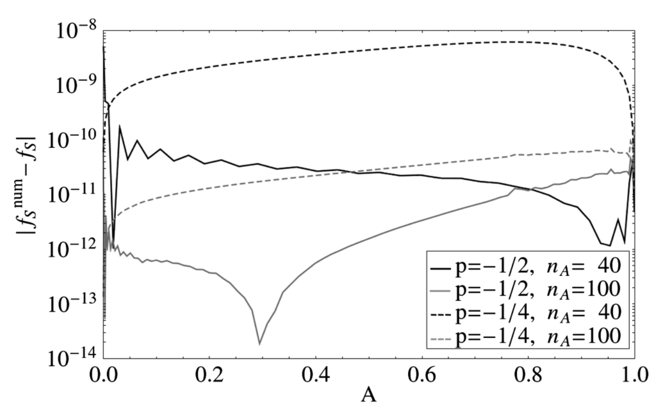

FIG. 3. Single $1 + \log$ trumpet, Schwarzschild solution. Absolute difference between the pseudospectral solution and the semianalytical result versus A for different values of p and n_A.

D. Multiple trumpets

Solving the Hamiltonian constraint for a regular conformal factor enables us to solve for the first time the Hamiltonian constraint for binary $1 + \log$ *trumpet* data. In contrast to the original puncture trick, where the generalization from one $1 + \log$ trumpet to two trumpets fails, using inverse powers of the conformal factor in the Hamiltonian constraint works without additional difficulties. Recall that our strategy is to postpone the solution of the momentum constraint, but we can still evaluate different approximation strategies for specifying the extrinsic curvature.

We decompose the extrinsic curvature according to $F = -K^2/12$ and $G = \bar{A}_{ij}\bar{A}^{ij}/8$ as we did for the single trumpet. This approach improves the stability of the code and decreases the residuum. Similar to the single trumpet we achieve only polynomial convergence. As a first ansatz we consider the following possibilities to specify F and G as a superposition of two single $1 + \log$ trumpets:

$$F = -\frac{1}{12}(K^2_{(1)} + K^2_{(2)}), \tag{37}$$

$$F = -\frac{1}{12}(K_{(1)} + K_{(2)})^2, \tag{38}$$

$$G = \frac{1}{8}(\bar{A}^{(1)}{}_{ij}\bar{A}_{(1)}{}^{ij} + \bar{A}^{(2)}{}_{ij}\bar{A}_{(2)}{}^{ij}), \tag{39}$$

$$G = \frac{1}{8}(\bar{A}^{(1)}{}_{ij} + \bar{A}^{(2)}{}_{ij})(\bar{A}_{(1)}{}^{ij} + \bar{A}_{(2)}{}^{ij}), \tag{40}$$

$$G = \frac{1}{8}(A^{(1)}_{ij}A^{ij}_{(1)} + A^{(2)}_{ij}A^{ij}_{(2)})\psi_0^{-12}, \tag{41}$$

where $\psi_0 = \psi_0^{(1)} + \psi_0^{(2)} - 1$ and $\psi_0^{(i)}$ are the solutions for single trumpets. We can use these simple superpositions since the source terms behave for large r like $F \sim r^{-8}$ and $G \sim r^{-6}$. Thus, for sufficient separation the effect of the superposition is negligible. Although we could add additional momentum, say of the BY type, as specified the two punctures are in an axisymmetric, head-on configuration, in which they are approximately at rest.

We tested all possible combinations of (37)–(41), and the code produces reasonable, and despite minor differences, similar results. As a particular example we consider two black holes with mass $m_1 = m_2 = m$ at a separation of $d = 2b = 12m$. In Fig. 4 we show for $p = -1/2$ the

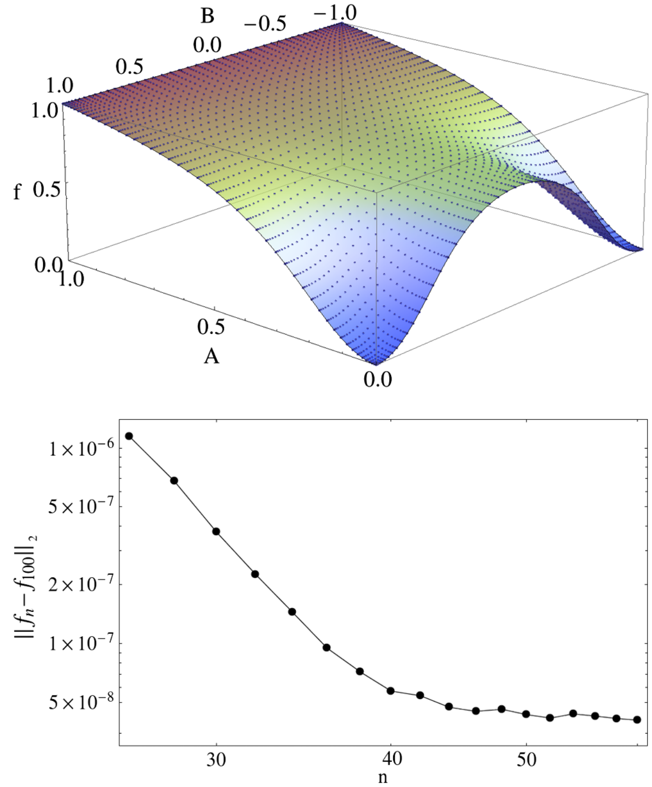

FIG. 4 (color online). Two $1 + \log$ trumpets, axisymmetric head-on case. The conformal factor f is shown for separation $d = 12m$ and masses $m_1 = m_2 = m$ using $p = -1/2$, (37), and (41) (upper panel). Also shown is the convergence of the error with $n = n_A = n_B$, for which we compute the l_2 norm of the difference to the solution for $n = 100$ (lower panel).

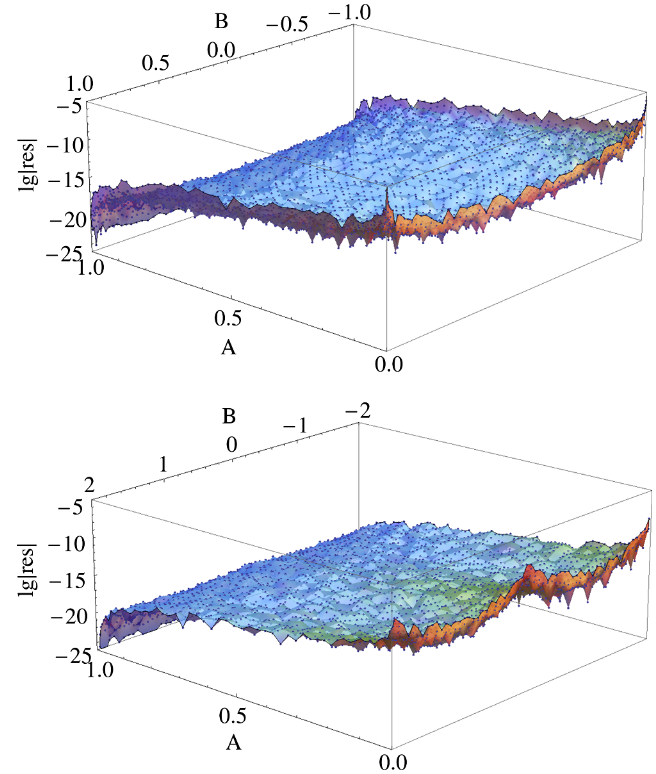

FIG. 5 (color online). Two $1 + \log$ trumpets as in Fig. 4. Logarithm of the absolute value of the residuum for two $1 + \log$ trumpets with $n_A = n_B = 60$, $n_\phi = 1$. The upper panel shows the result for the CCF configuration and the lower panel for CFF. Along the axis, which includes the punctures, the residuum is several orders of magnitude smaller for CFF than for CCF.

regular factor f using (37) and (41). We set $n = n_A = n_B$, and $n_\varphi = 1$ because of axisymmetry.

In the cases we tried, the CCF method (similar to [11]) was more robust than the CFF method; i.e. we could solve for a larger range of parameters with fewer grid points. For this reason we prefer the CCF grid and unless stated otherwise present results with this setup. On the other hand, the residuum for the CFF grid was smaller than for the CCF grid; see Fig. 5.

One of the features of $1 + \log$ trumpet initial data is the reduction of gauge dynamics. This reduction can be improved by a special choice of the initial shift and initial lapse for our evolutions, which is similar to choosing a precollapsed lapse for wormhole punctures. On the one hand, we can use a simple superposition

$$\alpha = \alpha_{(1)} + \alpha_{(2)} - 1 + \varepsilon, \tag{42}$$

$$\beta^i = \beta^i_{(1)} + \beta^i_{(2)}, \tag{43}$$

where ϵ is a small parameter to ensure that $\alpha > 0$ at the punctures. A coordinate dependent choice for ϵ is in principle possible, but was not tried in our investigations.

On the other hand, we can obtain lapse and shift by solving the corresponding equations of the conformal thin-sandwich (CTS) decomposition [38],

$$(\Delta_L \beta)^i = (L\beta)^{ij}\partial_j \ln(\alpha\psi^{-6}) + \frac{4}{3}\alpha\partial^i K, \tag{44}$$

$$\Delta(\alpha\psi) = \alpha\psi\left(\frac{7}{8}\psi^{-8}\bar{A}_{ij}\bar{A}^{ij} + \frac{5}{12}\psi^4 K^2\right) + \psi^5\beta^i\partial_i K, \tag{45}$$

where we use (42) and (43) for the computation of the source terms in the right-hand sides of the equations. Additionally, we have set $\partial_t K = \partial_t \bar{g}_{ij} = 0$ and denoted the vector Laplacian by Δ_L, while $(L\beta)^{ij} = \partial^i\beta^j + \partial^j\beta^i - \frac{2}{3}\bar{g}^{ij}\partial_k\beta^k$. Both ansatzes lead to approximately the same behavior in black hole evolutions. In Sec. IV we discuss results for (42) and (43), because they are easier to obtain and the difference between those results and results obtained with (44) and (45) seems to be minor.

IV. Evolution

The initial data are evolved with the BAM code [39–41] using the BSSN evolution scheme with $\tilde{\Gamma}$-driver shift and $1 + \log$ slicing.

A. Constraint violations

Evolutions of our trumpet data allow us to examine the effect of working with an *ad hoc* ansatz for the extrinsic curvature rather than solving the momentum constraint. Since we are not using maximal slicing, a simple superposition of the extrinsic curvature terms for single black holes is not a solution for the momentum constraint. The investigation of (37)–(41) revealed no significant difference in the constraint violation between (37) and (38). But minor differences depending on the superposition of G occurred, where (41) leads to the smallest constraint violation in our simulations. For evolutions, we define the initial extrinsic curvature by

$$\bar{A}_{ij} = \bar{A}^{(1)}_{ij} + \bar{A}^{(2)}_{ij}, \tag{46}$$

and raise indices with $\bar{g}^{ij}$ as usual, while in (39)–(41) indices are raised with the single puncture metric. *A priori* we do not know the momentum constraint violation, and from an analytical point of view it is quite debatable how well our ansatz will work. However, we find that the momentum constraint violation is dominated by the evolution itself and not by the inaccuracies of the initial data.

Equation (46) may lead to a large violation of the momentum constraint near the puncture. For simplicity we consider the initial guess for $\psi_0 = \psi_0^{(1)} + \psi_0^{(2)} - 1$. We assume $\psi_0^{(2)} - 1 = \xi \ll \psi_0^{(1)}$ near the first puncture. Then, the momentum constraint using the CTT decomposition and the conformal factor ψ_0 turns out to be

$$\partial_j \bar{A}^{ij} - \frac{2}{3}(\psi_0^{(1)} + \xi)^6 \bar{g}^{ij}\partial_j K \approx -4\xi(\psi_0^{(1)})^5 \bar{g}^{ij}\partial_j K_{(1)} \neq 0. \tag{47}$$

At the first puncture $\psi_0^{(1)} \to \infty$, which leads to a divergent constraint violation at the position of the first puncture.

However, evolutions with the puncture method are able to handle certain intrinsic regularity issues of the punctures, and in practice this is also the case for the momentum constraint violating initial data that we constructed. The question is how large the constraint violations are for evolutions of the approximate $1 + \log$ trumpet data compared to standard wormhole evolutions. As indicated by Fig. 6, the constraint violation has a comparable size, which suggests that the constraint violation produced by the evolution is the leading order effect. The black holes have a mass of m each and an initial separation of $d = 20m$, while the total (ADM) mass of the system is M. The l_2 norm was computed on the second outermost level with a grid spacing of $1M$, running from $-75M$ to $75M$.

B. Reduction of initial gauge dynamics

To quantify the reduction of initial gauge dynamics, we consider three different types of initial data: maximal wormholes, maximal trumpets, and $1 + \log$ trumpets.

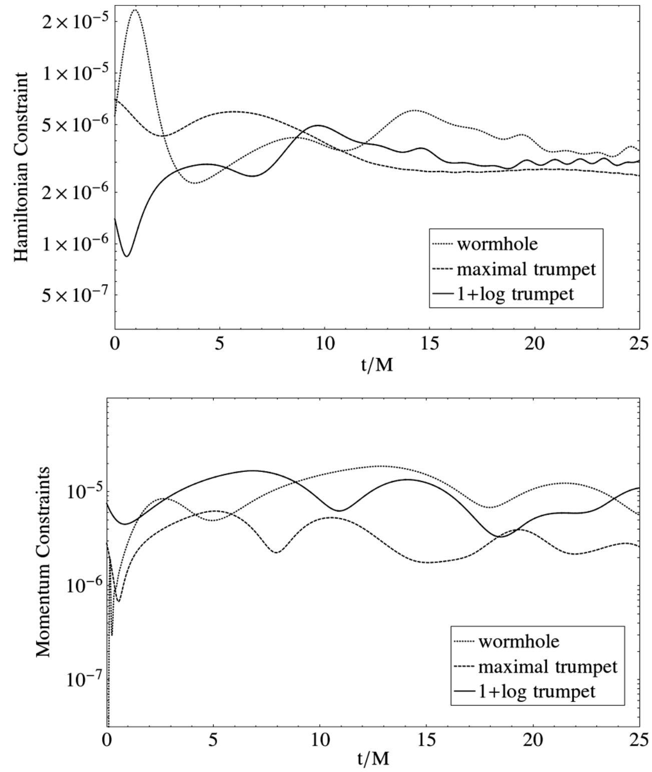

FIG. 6. Evolution of two black holes at the beginning of a head-on collision. Shown is the Hamiltonian constraint violation (upper panel) and norm of the momentum constraints (lower panel) for three types of initial data.

The results refer to an equal-mass binary black hole simulation with an initial separation of $d = 20m$, where the black holes are located on the x axis and perform a head-on collision. Additionally, we set $\eta = 0$ in the $\tilde{\Gamma}$-driver condition for this subsection to reduce the gauge-related growth of the coordinate distance of the apparent horizon [16,40,42].

We present two quantities which show that $1 + \log$ data are the preferred choice with respect to the initial gauge dynamics; see Fig. 7. First, we compute the change of the trace of the extrinsic curvature K during the beginning of the simulation. For this purpose we define the quantity

$$\mathcal{K} = \int_{x_{p_{i+1}}-\delta}^{x_{p_{i+1}}+\delta} K_{t_{i+1}} \mathrm{d}x - \int_{x_{p_i}-\delta}^{x_{p_i}+\delta} K_{t_i} \mathrm{d}x, \tag{48}$$

where $t_{i+1} - t_i = 0.125m$ and x_{p_i} is the position of the puncture for t_i. We choose $\delta = 2m$. Thus, we use a one-dimensional integral to measure the growth of K during the evolution. This is reasonable because the black holes initially are nearly spherical.

Second, we present the mean coordinate distance of the apparent horizon, which was already used in [19] to illustrate why maximal trumpets are a better choice for initial data than wormholes. In [19] the slicing condition

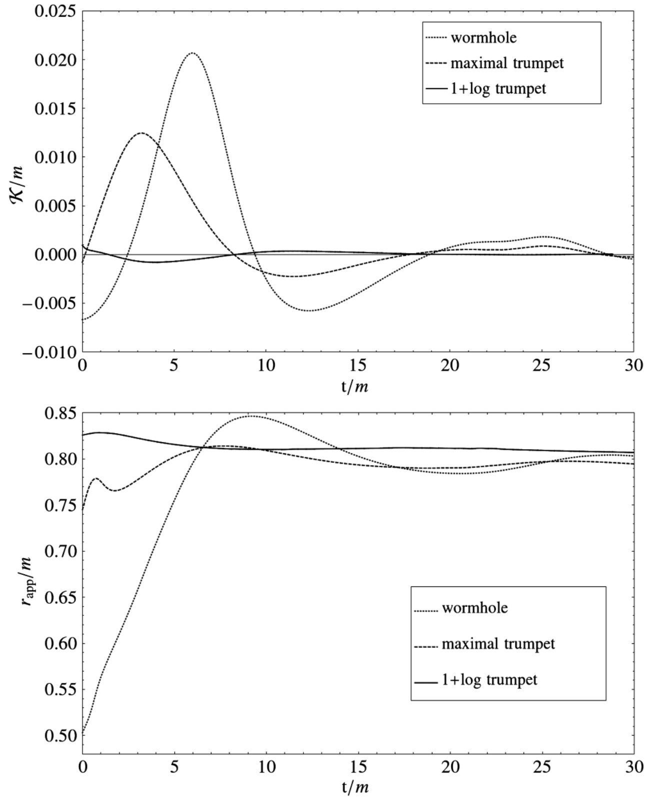

FIG. 7. Head-on collision of two black holes. Shown is $\mathcal{K}$ computed with Eq. (48) (upper panel) and the mean coordinate distance of the apparent horizon (lower panel). We have used (42) and (43) for the trumpet initial data and the precollapsed lapse $\alpha = \psi^{-2}$ for the wormholes. Using $\alpha = 1$ and $\beta^i = 0$ increases the gauge dynamics in all simulations.

$\partial_t \alpha = -2\alpha K$ was used so that after about $t = 10m$ the slicing was approximately maximal again. We will not use this equation as is, but instead include the shift term $\beta^i \partial_i \alpha$ on the right-hand side, since this is normally done in black hole simulations.

Regarding the upper panel of Fig. 7, we conclude that the initial change of K is reduced by our $1 + \log$ trumpets. There are two reasons for the nonvanishing $\mathcal{K}$ found for our data. On the one hand, there still exist small gauge dynamics at the beginning of the simulation, while, on the other hand, $\mathcal{K} \neq 0$ because of the evolution itself. During the evolution the linear momentum of the black hole is increasing, which leads to a small decrease in K. However, it is obvious that because of the initial change from maximal to $1 + \log$ slicing there has to be a change in K (from zero to nonzero) for the wormholes and the maximal trumpets. Therefore, we present the mean coordinate distance of the apparent horizon as a second diagnostic of the initial gauge dynamics. The lower panel of Fig. 7 reveals the same behavior found before, namely the $1 + \log$ trumpet is the preferred choice to minimize the early gauge dynamics of the evolution. The initial dynamics of the horizon radius is reduced for the $1 + \log$ trumpet

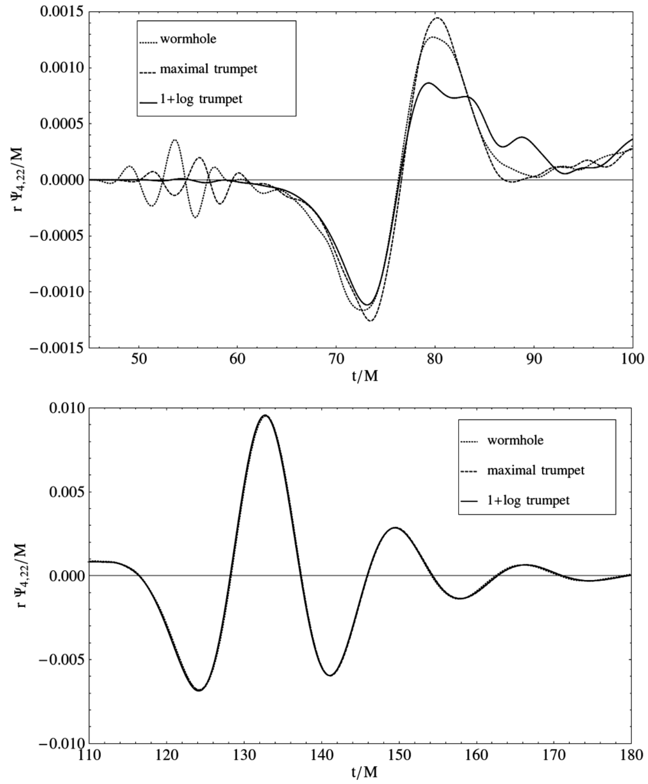

FIG. 8. Head-on collision of two black holes. Shown is the junk radiation (upper panel) and the gravitational wave signal at later times (lower panel). The time coordinate is shifted in such a way that characteristic points coincide.

compared to the maximal trumpet, although on the given scale there is not much difference between the two types of trumpet data.

C. Junk radiation and the gravitational wave signal

Since we are using conformally flat initial data, we do not avoid the production of junk radiation. This issue was discussed for maximal trumpets in [19], and analogous arguments hold also for $1 + \log$ trumpets. Figure 8 shows the gravitational radiation from the head-on collision of two punctures starting at $d = 20m \approx 10M$ in terms of the spin-weight -2, $l = 2$, $m = 2$ mode of $r\Psi_4$ computed at an extraction radius of $r_{\rm ex} = 75M$. The amount of junk radiation (upper panel) for wormholes and trumpets is approximately the same. The figure suggests that some features of the early wave pulse are due to conformal flatness, while others (the leading oscillations for wormhole data that are absent from $1 + \log$ trumpet data) may be residues of the early gauge dynamics. Figure 8 can be compared with Fig. 12 of [19], which shows a similarly small difference in the junk radiation between a maximal trumpet and a wormhole, including small oscillations for wormhole data. A significant reduction of junk radiation can be achieved by computing nonconformally-flat initial data, e.g. [43–48].

Another important question is whether the different types of initial data describe the same physical system. For this purpose we have a closer look at the gravitational wave signal at later times in Fig. 8 (lower panel). The physically relevant part of the gravitational wave signal is nearly identical on this scale.

There are two obvious reasons why the signals cannot be identical. First, we have not solved the momentum constraint, and therefore we use a setup that deviates slightly from an exact solution of Einstein's field equations. Second, using the same bare initial masses for wormholes, maximal trumpets, and $1 + \log$ trumpets leads to different ADM masses. We can rescale by the ADM mass M, but this leads to small differences in the rescaled initial separation. However, the results agree quite well even without fine-tuning.

V. CONCLUSION

The aim of this paper was to solve the Hamiltonian constraint for $1 + \log$ trumpets, as opposed to maximal trumpets or wormholes. Since $1 + \log$ trumpet initial data are constructed in the approximately stationary, quasiequilibrium gauge of evolutions using the standard moving puncture method, such initial data are a natural choice that can be expected to minimize the initial gauge dynamics.

As a general strategy to address a pole singularity in the conformal factor, we suggest considering negative powers of the conventional conformal factor; see also [20,25,34]. In fact, the original additive puncture method fails for $1 + \log$ trumpet punctures, while we showed that regularizing the conformal factor by using its inverse succeeds both for wormholes and trumpets. Note that the character of the Hamiltonian constraint equation is different for wormholes, maximal trumpets, and $1 + \log$ trumpets. The novelty of the present work is a working scheme for the superposition of two $1 + \log$ Schwarzschild trumpets, which is the first treatment of the $K \neq 0$ case in this context.

One open issue is the *ad hoc* approach to the momentum constraint, for which various approximate solutions were constructed. It is encouraging that in actual evolutions the violation of the momentum constraint reached comparable levels even for constraint-solved wormhole data. The evolutions also indicated that the $1 + \log$ trumpet data indeed contain fewer artifacts. It remains to be investigated whether similar methods can be applied to the solution of the momentum constraint.

With the basic superposition of two $1 + \log$ Schwarzschild trumpets available, a follow-up project is the inclusion of momentum and spin. This can in principle be achieved by adding Bowen-York extrinsic curvature to the (nonvanishing) extrinsic curvature of the head-on $1 + \log$ trumpet configuration. However, to avoid the artificial radiation in Bowen-York data, we would prefer a method that is based on the quasiequilibrium state of orbiting trumpets in the moving puncture gauge.

Part of this exercise is academic because wormhole punctures quickly and reliably evolve into quasistationary $1 + \log$ punctures. There are advantages if the early part of the waveform is important, but this may not be essential in practical terms. Still, from a theoretical point of view, constructing moving puncture initial data is worthwhile since it would resolve the puzzling state of affairs that one of the most successful slicings of binary black spacetimes can currently only be found by performing actual evolutions, without having an approximate initial data construction available.

ACKNOWLEDGMENTS

It is a pleasure to thank M. Ansorg, D. Hilditch, and J. Gundermann for helpful discussions. We are grateful to T. Baumgarte and N. K. Johnson-McDaniel for comments on the manuscript. This work was supported in part by DFG grant SFB/Transregio 7 "Gravitational Wave Astronomy." T. D. was supported by the Graduierten-Akademie Jena and the Studienstiftung des deutschen Volkes. Computations were performed at the Quadler cluster of the Institute of Theoretical Physics of the University of Jena and on SuperMUC of the Leibniz Rechenzentrum.

[1] E. Seidel and W.-M. Suen, Phys. Rev. Lett. **69**, 1845 (1992).
[2] S. Brandt and B. Brügmann, Phys. Rev. Lett. **78**, 3606 (1997).
[3] M. Campanelli, C. O. Lousto, P. Marronetti, and Y. Zlochower, Phys. Rev. Lett. **96**, 111101 (2006).
[4] J. G. Baker, J. Centrella, D.-I. Choi, M. Koppitz, and J. van Meter, Phys. Rev. Lett. **96**, 111102 (2006).
[5] B. Brügmann, Int. J. Mod. Phys. D **08**, 85 (1999).
[6] M. Shibata and T. Nakamura, Phys. Rev. D **52**, 5428 (1995).
[7] T. W. Baumgarte and S. L. Shapiro, Phys. Rev. D **59**, 024007 (1998).
[8] C. Bona, J. Massó, E. Seidel, and J. Stela, Phys. Rev. Lett. **75**, 600 (1995).
[9] M. Alcubierre, B. Brügmann, D. Pollney, E. Seidel, and R. Takahashi, Phys. Rev. D **64**, 061501(R) (2001).
[10] M. Alcubierre, B. Brügmann, P. Diener, M. Koppitz, D. Pollney, E. Seidel, and R. Takahashi, Phys. Rev. D **67**, 084023 (2003).
[11] M. Ansorg, B. Brügmann, and W. Tichy, Phys. Rev. D **70**, 064011 (2004).
[12] J. D. Brown and L. L. Lowe, J. Comput. Phys. **209**, 582 (2005).

[13] M. Hannam, S. Husa, D. Pollney, B. Brügmann, and N. Ó Murchadha, Phys. Rev. Lett. **99**, 241102 (2007).
[14] J. D. Brown, Phys. Rev. D **77**, 044018 (2008).
[15] M. Hannam, S. Husa, N. Ó Murchadha, B. Brügmann, J. A. González, and U. Sperhake, J. Phys. Conf. Ser. **66**, 012047 (2007).
[16] M. Hannam, S. Husa, F. Ohme, B. Brügmann, and N. Ó Murchadha, Phys. Rev. D **78**, 064020 (2008).
[17] T. W. Baumgarte and S. G. Naculich, Phys. Rev. D **75**, 067502 (2007).
[18] J. D. Immerman and T. W. Baumgarte, Phys. Rev. D **80**, 061501 (2009).
[19] M. Hannam, S. Husa, and N. Ó Murchadha, Phys. Rev. D **80**, 124007 (2009).
[20] T. W. Baumgarte, Phys. Rev. D **85**, 084013 (2012).
[21] L. T. Buchman, H. P. Pfeiffer, and J. M. Bardeen, Phys. Rev. D **80**, 084024 (2009).
[22] T. W. Baumgarte, Z. B. Etienne, Y. T. Liu, K. Matera, N. Ó Murchadha, S. L. Shapiro, and K. Taniguchi, Classical Quantum Gravity **26**, 085007 (2009).
[23] J. W. York, Jr., in *Sources of Gravitational Radiation* edited by L. Smarr (Cambridge University Press, Cambridge, UK, 1979), pp. 83–126.
[24] J. M. Bowen and J. W. York, Jr., Phys. Rev. D **21**, 2047 (1980).
[25] J. Gundermann, Diploma thesis, University of Jena, 2010.
[26] T. W. Baumgarte, Classical Quantum Gravity **28**, 215003 (2011).
[27] M. Ansorg and S. Bai (private communication).
[28] R. Beig and N. O'Murchadha, Classical Quantum Gravity **11**, 419 (1994).
[29] R. Beig and N. O'Murchadha, Classical Quantum Gravity **13**, 739 (1996).
[30] S. Dain and H. Friedrich, Commun. Math. Phys. **222**, 569 (2001).
[31] P. Galaviz, B. Brügmann, and Z. Cao, Phys. Rev. D **82**, 024005 (2010).
[32] F. Ohme, Diploma thesis, University of Jena, 2008.
[33] B. Brügmann, Gen. Relativ. Gravit. **41**, 2131 (2009).
[34] T. Dietrich, Master thesis, University of Jena, 2012.
[35] P. E. Merilees, Atmosphere **11**, 13 (1973).
[36] B. Fornberg, *A Practical Guide to Pseudospectral Methods* (Cambridge University Press, Cambridge, UK, 1998).
[37] B. Brügmann, J. Comput. Phys. **235**, 216 (2013).
[38] J. W. York, Phys. Rev. Lett. **82**, 1350 (1999).
[39] S. Husa, J. A. González, M. Hannam, B. Brügmann, and U. Sperhake, Classical Quantum Gravity **25**, 105006 (2008).
[40] B. Brügmann, J. A. González, M. Hannam, S. Husa, U. Sperhake, and W. Tichy, Phys. Rev. D **77**, 024027 (2008).
[41] B. Brügmann, W. Tichy, and N. Jansen, Phys. Rev. Lett. **92**, 211101 (2004).
[42] D. Müller, J. Grigsby, and B. Brügmann, Phys. Rev. D **82**, 064004 (2010).
[43] W. Tichy, B. Brügmann, M. Campanelli, and P. Diener, Phys. Rev. D **67**, 064008 (2003).
[44] N. Yunes, W. Tichy, B. J. Owen, and B. Brügmann, Phys. Rev. D **74**, 104011 (2006).
[45] G. Lovelace, R. Owen, H. P. Pfeiffer, and T. Chu, Phys. Rev. D **78**, 084017 (2008).
[46] G. Lovelace, Classical Quantum Gravity **26**, 114002 (2009).
[47] B. J. Kelly, W. Tichy, Y. Zlochower, M. Campanelli, and B. F. Whiting, Classical Quantum Gravity **27**, 114005 (2010).
[48] G. Reifenberger and W. Tichy, Phys. Rev. D **86**, 064003 (2012).